Simultaneous Measurement of Dual Parameters Based on Periodically Embedding MMF-Induced Ultralong-Period Fiber Grating

Jiabin Wang, Jian Zhou, Jiayu Hao, Xinzhe Zeng, Wenhuan Chen, Yue Liu, Haoran Meng, Jinghua Sun, Tao Geng, and Weimin Sun

***Abstract*—In this article, an ultralong period fiber grating (ULPFG) based on periodically embedding multimode fiber into single mode fiber (PEM-ULPFG) is proposed to simultaneously measure the liquid refractive index (RI) and temperature with high sensitivity. Five resonant dips belong to different cladding modes, and diffraction mode orders appear in the transmission spectrum. The responses of the dips to RI and temperature are different. Therefore, high sensitivity and dual-parameter measurement are realized. Numerical simulation based on the beam propagation method (BPM) is also carried out to design and optimize the parameters of the device. Experimental results show that the maximum RI sensitivity of −1230 nm/RIU in the range of 1.4021–1.4383 RIU is achieved by tracing the target dip (dip 4). The temperature response of dip 4 is also characterized to be as low as 52.6 pm/°C. Another dip (dip 5) is used for measuring temperature with the temperature sensitivity of 92.3 pm/°C. Different responses to the external changes of the dips obtained by the PEM-ULPFG make the proposed sensor competitive in the field of high sensitivity and dual-parameter sensing.**

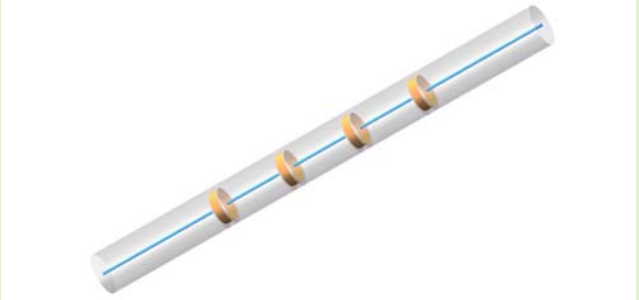

***Index Terms*— Refractometer, simultaneous measurement, ultralong-period fiber grating (ULPFG).**

I. Introduction

IN THE fields of biochemistry, industrial product testing, and environmental monitoring [1], [2], [3], it is important to measure physical parameters like temperature, refractive index (RI), and humidity [4], [5], [6]. In recent years, fiber sensors based on Mach–Zehnder interferometer (MZI) [7], Fabry–Perot interferometer (FPI) [8], fiber Bragg grating (FBG) [9], long period fiber grating (LPFG), and ultralong period fiber grating (ULPFG) [10] have been widely studied and deployed in practical applications. Although optical fiber grating sensors for detecting changes in RI in the external environment have been widely studied, there are still some problems such as the sensitivity of the fiber gratings being influenced by the temperature [11], [12]. ULPFGs are considered potential candidates for two-parameter measurement due to the different responses of the resonant dips [13], [14].

There are various methods for manufacturing ULPFGs, including the laser writing method with UV exposure [15], CO_2 laser etching, and femtosecond laser embossing [16], [17], and nonlaser writing method with arc bulging [18], resistive filament heating [19], mechanical microbending [20], and staggered core splicing [21]. The laser writing method has the advantages of good repeatability, fast etching time, and accurate control of RI modulation, but it requires expensive instruments. The nonlaser writing method does not depend on expensive equipment, but the production accuracy and repeatability are hard to be guaranteed, and the process is time-consuming and complicated. In addition, ULPFGs fabricated by the nonlaser writing method always have relatively low sensitivity. Various functional materials have been

Manuscript received 15 November 2022; accepted 2 December 2022. Date of publication 9 December 2022; date of current version 12 January 2023. This work was supported in part by the State Key Laboratory of Applied Optics under Grant SKLA02022001A02, in part by the Joint Research Fund in Astronomy under Cooperative Agreement between the National Natural Science Foundation of China (NSFC) and the Chinese Academy of Sciences (CAS) under Grant U2031132 and Grant U2031130, and in part by the Fundamental Research Funds for the Central Universities to Harbin Engineering University. The associate editor coordinating the review of this article and approving it for publication was Dr. Daniele Tosi. *(Corresponding author: Tao Geng.)*

Jiabin Wang, Jian Zhou, Jiayu Hao, Xinzhe Zeng, Wenhuan Chen, Yue Liu, and Weimin Sun are with the Key Laboratory of In-Fiber Integrated Optics, Ministry Education of China, Harbin Engineering University, Harbin 150001, China.

Haoran Meng is with the Changchun Institute of Optics, Fine Mechanics and Physics, Chinese Academy of Sciences, Changchun 130033, China.

Jinghua Sun is with the College of Physics and Optoelectronic Engineering, Harbin Engineering University, Harbin 150001, China.

Tao Geng is with the Key Laboratory of In-Fiber Integrated Optics, Ministry Education of China, Harbin Engineering University, Harbin 150001, China, and also with the State Key Laboratory of Applied Optics, Changchun Institute of Optics, Fine Mechanics and Physics, Chinese Academy of Sciences, Changchun 130033, China (e-mail: gengtao_hit_oe@126.com).

Digital Object Identifier 10.1109/JSEN.2022.3226863

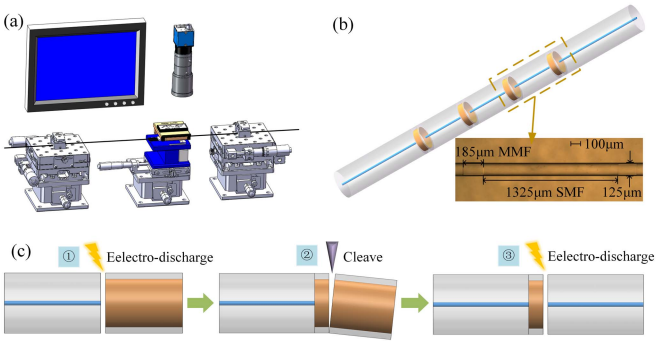

Fig. 1. (a) Schematic of the experimental setup. (b) Schematic of PEM-ULPFG structure. (c) PEM-ULPFG production process.

deposited on the sensor to enhance the sensing performance. For example, Song et al. [22] used HGFI to modify the hydrophobic characteristics of conical ULPFG surface and improved the performance of immune biosensing. But its manufacture is complicated and its stability is poor. Therefore, it is important to design fiber sensors for simultaneously measuring dual parameters such as RI and temperature with high sensitivity and dynamic range.

In this article, alternately cleaving and splicing SMF and MMF technique is used first to fabricate ULPFGs for high-sensitivity RI and temperature measurements. Periodical-embedded MMF (PEM) is able to induce the coupling between the fundamental mode and the copropagating cladding modes within relatively fewer period numbers. Periodically embedding multimode fiber-induced ULPFGs (PEM-ULPFGs) with four periods are designed and fabricated. Five resonant dips appear in the wavelength range of 1000–1700 nm. Numerical simulation not only describes the light propagation in the device, but also shows that the five dips belong to different cladding mode orders. Experimental results show that an ordinary RI sensitivity of −294.2 nm/RIU in the range of 1.3333–1.4021 RIU and a maximum sensitivity of −1230 nm/RIU in the range of 1.4021–1.4383 RIU is achieved by tracing the target dip (dip 4). Another dip (dip 5) is traced for measuring temperature whose temperature sensitivity is 92.3 pm/°C. The maximum RI sensitivity of dip 5 is only −675.5 nm/RIU (1.4021–1.4383 RIU) which is only about half of dip 4. Using a matrix equation, simultaneous measurement of RI and temperature with high sensitivity is achieved. Compared with conventional LPFGs and fiber-optic interferometers, the proposed PEM-ULPFG has the advantages of simple preparation, high sensitivity, large dynamic range, and high mechanical strength. In addition, all the parameters are able to be optimized through numerical simulation, which endows the device with flexible designability.

II. Device Preparation

For fabricating the PEM-ULPFG, SMF with core/cladding diameter of 8.3/125 μm (SMF-28e+, Corning) and MMF with core/cladding diameter of 105/125 μm (105/125-22/250, YOFC) are used. The precision cutting system for fabricating the device is shown in Fig. 1(a). The fiber is held by a pair of fixtures. A commercial optical fiber cleaver is placed on a 3-D translation platform. The schematic and micrograph of the PEM-ULPFG are shown in Fig. 1(b). The preparation steps are shown in Fig. 1(c). First, the SMF and MMF with flat cut ends were discharge welded with a commercial fiber fusion splicer FSM-62C (Fujikura Company Ltd.) to ensure that each welding loss is less than 0.3 dB. The key parameters of the splicer are set as, discharge time: 3000 ms, standard heating power, and overlap 6 μm, respectively. Second, the semi-finished device is placed on the precision cutting system. The displacement stage is able to precisely move the fiber cleaver. And with the help of the microscope with CCD, the fiber can be cut at a certain length with a cutting error of less than 1 μm [14]. Finally, the fiber is spliced to the SMF again, and the process of splicing–cutting–splicing is repeated to obtain a four-period PEM-ULPFG. In the experiment, the length of the SMF and the MMF in a period are 185 and 1325 μm, respectively. It means that the period length is 1510 μm. The overall length of the sensor is 6040 μm.

III. Principle and Simulation

The period of the PEM-ULPFG is 1510 μm, which is larger than that of a normal LPFG. The PEM-ULPFG is also a transmission grating. While, unlike the LPFG, the core fundamental mode also couples with the forward transmitted higher-order diffraction mode [23]. According to the coupling mode theory, the relative phase-matching condition of the PEM-LPFG is expressed as

$$\lambda_D^{N,m} = \left(n_{\text{eff}}^{\text{co}} - n_{\text{eff}}^{\text{cl},N,m}\right)\Lambda/N \tag{1}$$

where Λ is the grating period and N is the diffraction mode order. For an ordinary LPFG, $N = 1$. $\lambda_D^{N,m}$ is the designed resonant wavelength, $n_{\text{eff}}^{\text{cl},N,m}$, and $n_{\text{eff}}^{\text{co}}$ denote the effective RI of the Nth-order diffraction mode of the mth-order cladding mode and the fundamental mode, respectively. According to (1), the shorter-wavelength resonance dip corresponds to a higher diffraction level. Disregarding the effect of fiber dispersion, the actual resonant wavelength of PEM-ULPFG is

$$\lambda_{\text{res}}^{N,m} = \left(n_{\text{eff}}^{\text{co}} - n_{\text{eff}}^{\text{cl},N,m}\right)\Lambda/N \times \left[1 + \frac{\left(\delta n_{\text{eff}}^{\text{co}} - \delta n_{\text{eff}}^{\text{cl},N,m}\right)\cdot d\lambda_D/d\Lambda}{\left(n_{\text{eff}}^{\text{co}} - n_{\text{eff}}^{\text{cl},N,m}\right)^2}\right] \tag{2}$$

where $\lambda_{\text{res}}^{N,m}$ is the actual resonant wavelength and $n_{\text{eff}}^{\text{cl},N,m}$ and $n_{\text{eff}}^{\text{co}}$ denote the effective RI change of the m^{th}-order cladding mode under the Nth-order diffraction mode and the fundamental mode, respectively. Considering the influence of the fusion spliced process, $n_{\text{eff}}^{\text{co}}$ and $n_{\text{eff}}^{\text{cl},N,m}$ are expressed as

$$\delta n_{\text{eff}}^{\text{co(cl},N,m)} = \delta n_{\text{residual}} + \delta n_{\text{density}} + \delta n_{\text{expansion}} \tag{3}$$

where $\delta n_{\text{residual}}$ is the disturbance caused by the residual stress relaxation due to the high temperature generated by the arc discharge, $\delta n_{\text{density}}$ is the perturbation caused by the material density, and $\delta n_{\text{expansion}}$ is the perturbation caused by the expansion of the fiber core diameter. From (2), it is

clear that different resonance dips of the transmission spectrum of the PEM-ULPFG have different sensitivity to the external environmental changes since N and m of the cladding modes are different. The sensitivity characteristics of PEM-ULPFGs to environmental RI are derived from the following equation:

$$\frac{d\lambda_{\text{res}}^{N,m}}{dn_e} = \frac{d\lambda_{\text{res}}^{N,m}}{dn_{\text{eff}}^{c,N,m}} \cdot \frac{dn_{\text{eff}}^{\text{cl},N,m}}{dn_e} = -\frac{\Lambda}{N} \cdot \frac{d\lambda_{\text{res}}^{N,m}(n_{\text{cl}}, n_e)}{dn_e} \quad (4)$$

where n_e and n_{cl} are the RI of the environment and the fiber cladding, respectively. When $n_e < n_{cl}$ and $d\lambda_{\text{res}}^{N,m} < 0$, the resonant wavelength is blue-shifted with surrounded RI increased. Similarly, we obtained the temperature sensitivity of the PEM-ULPFG

$$\begin{aligned}\frac{d\lambda_{\text{rs}}^{N,m}}{dT} &= \lambda_{\text{rs}}^{N,m} N \frac{\left(d\lambda_{\text{res}}^{N,m}/d\Lambda\right)\left(\alpha + \xi_{\text{co}} n_{\text{eff}}^{\text{co}} - \xi_{\text{cl}} c_{\text{eff}}^{\text{cl},N,m}\right)}{\left(n_{ef}^{\text{co}} - n_{\text{eff}}^{\text{cl},N,m}\right)^2} \\ &= \left(n_{\text{eff}}^{\text{co}} - n_{\text{eff}}^{\text{cl},N,m}\right)\Lambda\left[1 + \frac{\left(\delta n_{\text{eff}}^{\text{co}} - \delta n_{ef}^{\text{cl},N,m}\right)\cdot d\lambda_D/d\Lambda}{\left(n_{\text{eff}}^{\text{co}} - n_{ef}^{\text{cl},N,m}\right)^2}\right] \\ &\quad \cdot \frac{\left(d\lambda_{\text{rs}}^{N,m}/d\Lambda\right)\left(\alpha + \xi_{cc} n_{\text{eff}}^{\text{co}} - \xi_{\text{cl}} l_{\text{eff}}^{c,N,N,m}\right)}{\left(n_{\text{eff}}^{\text{co}} - n_{ef}^{\text{cl},N,m}\right)^2} \end{aligned} \quad (5)$$

where α is the thermal expansion coefficient (TEC) of the fiber, and ξ_{co} and ξ_{cl} are the thermo-optical coefficients (TOCs) of the fiber core and cladding, respectively. From (5), $\lambda_{\text{rs}}^{N,m}$ is inversely proportional to N. The temperature sensitivity of MMF-LPFGs is independent of the diffraction order, which is constant for the same cladding mode but different diffraction order modes [15]. In addition, the temperature sensitivity of the resonance dip is different for different wavelengths due to different cladding modes.

Numerical simulation based on the beam propagation method (BPM) is carried out to reveal the transmission spectra and light propagation in the PEM-ULPFG. In the simulation, the core/cladding diameters of MMF and SMF are 105/125 and 8.3/125 μm, respectively. The RI of the core/cladding RI of MMF and SMF are 1.4628/1.444 and 1.4501/1.444 RIU, respectively. The mesh size is 0.2 μm in the XY-direction and 1 μm in the Z-direction. As shown in Fig. 2(a), there is a strong energy exchange between the core and cladding during transmission due to the severe mismatch of core diameters between MMF and SMF. Therefore, MMF can reduce the number of cycles for shorter sensor lengths. As shown in Fig. 2(b), the five main resonance dips obtained by simulation are at 1091.7, 1185.8, 1290.5, 1451.2, and 1640.6, respectively. The deviation between simulation results and experimental results is caused by the welding process.

As shown in Fig. 2(c), dip 3, dip 4, and dip 5 are selected for simulation according to actual needs, and the mode field is obtained. Dip 3 (^{2}LP$_{013}$) and dip 4 (^{4}LP$_{012}$) have lower cladding mode order than dip 5 (^{2}LP$_{016}$), and dip 4 (^{4}LP$_{012}$) has the highest diffraction order according to the theory mentioned in [15].

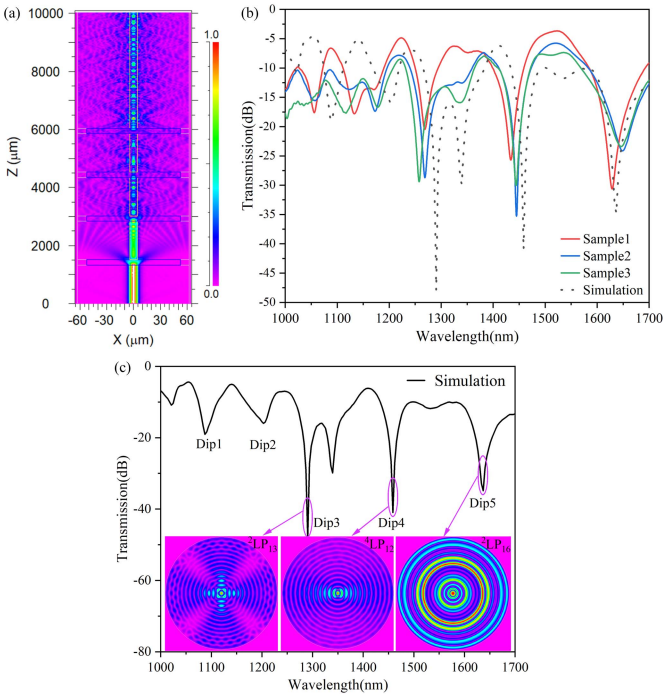

Fig. 2. (a) Energy distribution of light wave in the PEM-ULPFG. (b) Transmission spectra of PEM-ULPFG. (c) Simulated mode field of the PEM-ULPFG of dip 3 and dip 5. The resonance of the cladding mode of the mth order with diffraction order N in the figure is expressed as ^{N}LP$_{0m}$.

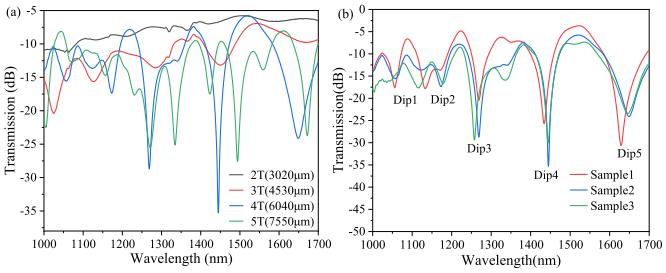

Fig. 3. (a) Transmission spectra with periods of 2, 3, 4, and 5. (b) Transmission spectra of three samples with the same parameters.

IV. Experiment and Discussion

Fig. 3(a) shows the experimental transmission spectrum evolution of the PEM-ULPFG with periods number from 2 to 5. For a PEM-ULPFG with two periods, the phase matching condition is not satisfied, and no resonant dips appear. For the device with three periods, there are five resonance dips with a relatively low extinction ratio (ER) of about 5 dB. For the device with five periods, too many resonant dips appear in the spectrum, which is not suitable for practical applications. And four periods produce the best resonance dips.

In order to verify the repeatability of the device, three more samples with the same parameters have been fabricated. Their transmission spectra are shown in Fig. 3(b). The slight variation of the resonant wavelength and the related ER are caused by the length errors of the SMF section or MMF section. Meanwhile, the electrode aging of the fusion splicer

TABLE I
RESPONSES OF THE TARGET RESONANT DIPS TO RI

Dip number	Linear fitting function	RI sensitivity(nm/RIU)	R^2	Measurement range (RIU)
3	$y = -182.1x + 1503.9$	-182.1	0.98	$1.3333 - 1.4021$
	$y = -405.5x + 1817.8$	-405.5	0.95	$1.4021 - 1.4383$
4	$y = -294.2x + 1826.4$	-294.2	0.97	$1.3333 - 1.4021$
	$y = -1230x + 3139.1$	-1230	0.98	$1.4021 - 1.4383$
5	$y = -263.9x + 1980$	-263.9	0.99	$1.3333 - 1.4021$
	$y = -675.5x + 2556.4$	-675.5	0.99	$1.4021 - 1.4383$

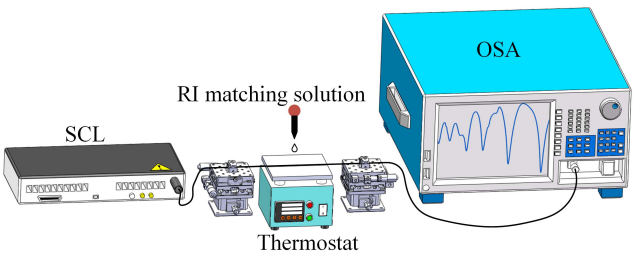

Fig. 4. Schematic of the RI and temperature measurement device.

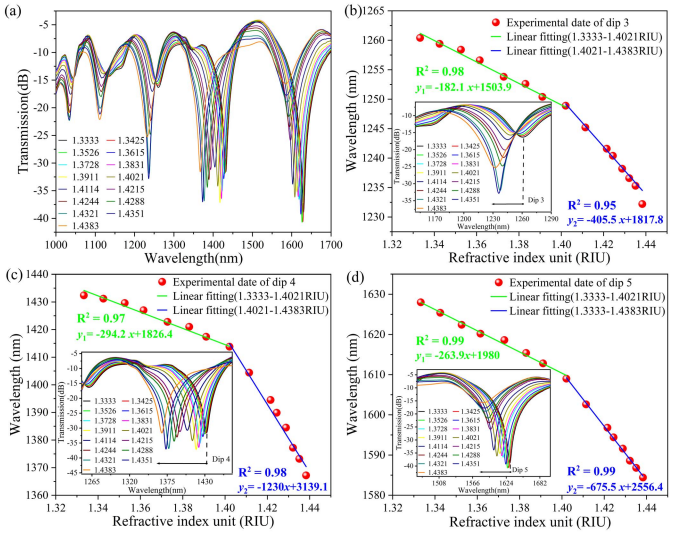

Fig. 5. (a) Wavelength shift of PEM-ULPFGs at different RI; RI response of different resonance dips (b) dip 3, (c) dip 4, and (d) dip 5.

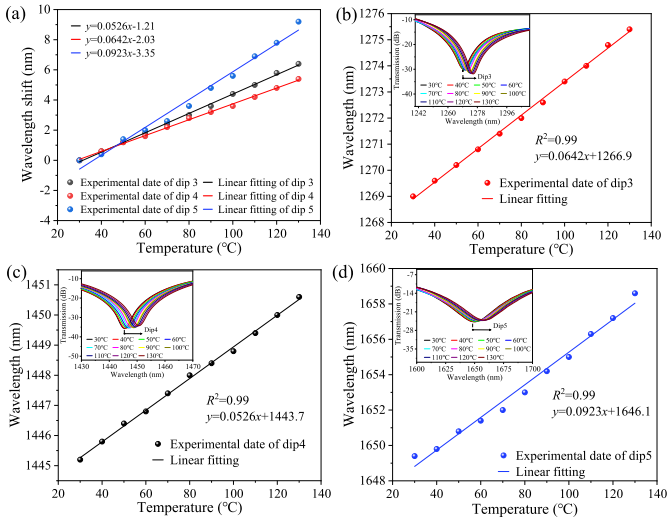

Fig. 6. (a) Wavelength drift of PEM-ULPFGs at different temperatures; temperature response of different resonance dips (b) dip 3, (c) dip 4, and (d) dip 5.

also influences the $\delta n_{\text{residual}}$, $\delta n_{\text{density}}$, and $\delta n_{\text{expansion}}$ in (3). But the subtle difference is acceptable.

Fig. 4 shows the schematic of the RI and temperature measurement device. The supercontinuum light source (SCL) SC-5 (YSL Photonics Company Ltd.) produces continuous light in the wavelength range of 1000–1700 nm. An optical spectrum analyzer (OSA) AQ6370D (YOKOGAWA Company Ltd.) with a resolution of 0.02 nm records the transmission spectra. The sensor is held by a pair of fixtures. The RI sensitivity is measured at room temperature (25 °C). Calibrate index-matching solutions with RI from 1.3333 to 1.4383 RIU is prepared by the aqueous solution of glycerol with different concentrations. The power of the thermostat is disconnected. Different index-matching solutions are dripped to the sensor. The transmission spectra recorded by the OSA are shown in Fig. 5(a).

As is analyzed in Section III, the resonance dip is blue-shifted with the RI increased. Fig. 5(b)–(d) shows the RI responses of dip 3–dip 5, respectively. The RI sensitivity at different dips of the sensor is obtained by linear fitting. The results are listed in Table I.

The RI sensitivities of the target dips are different due to the different diffraction orders and cladding mode orders they belong. A segmented linear function is used to fit the relationship between the RI changes and the resonant wavelength shift. In the range of 1.3333–1.4383 RIU, dip 4 exhibits the highest RI sensitivity (−1230 nm/RIU) among the three target dips. As a result, dip 4 is selected to measure the surrounded RI.

The temperature response of the sensor is also characterized using a constant temperature furnace in the temperature range from 30 °C to 130 °C. We recorded the transmission spectra every 10 °C. The resonant dips shift to a longer wavelength with the increased temperature. The temperature sensitivity is obtained using linear fitting. The spectrum evolution of the three target dips and the linear fitting results are depicted from Fig. 6(a)–(d). The temperature response function and the goodness of fitting are listed in Table II. The different temperature sensitivity of the three dips is caused by their different cladding mode orders, but the difference in diffraction order does not affect the temperature sensitivity.

We note that although the temperature sensitivity is similar, the RI sensitivity of the five dips a different. Considering

TABLE II
RESPONSE RESULTS OF THREE RESONANT DIPS TO TEMPERATURE

Dip number	Linear fitting function	Temperature sensitivity (nm/°C)	R^2	Measurement range (°C)
3	$y = 0.0642x + 1287.1$	0.0642	0.99	30-130
4	$y = 0.0526x + 1447.5$	0.0526	0.99	30-130
5	$y = 0.0923x + 1653.8$	0.0923	0.99	30-130

TABLE III
CHARACTERISTICS OF FIBER SENSORS FOR DUAL-PARAMETER MEASUREMENT

Structure	RI sensitivity (nm/RIU)	Temperature sensitivity (pm/°C)	Number of periods	Dynamic range (RIU)
Side-throw induced MZI [7]	730.5	15	-	1.33-1.42
SFT-MZI cascaded LPFG [24]	311.48	45.87	60	1.333-1.372
CO_2 laser induced ULPFG [13]	741	78	16	1.43-1.45
Femtosecond laser induced ULPFG [17]	626.4	110	25	1.412-1.454
Present work	**-294.2& -1230**	**92.3**	**4**	**1.333-1.4021& 1.4021-1.4383**

the practical applications and the costs, we choose dip 4 (at 1444.6 nm) to measure the RI and dip 5 (at 1649.2 nm) to monitor the temperature changes.

To realize the dual-parameter measurement, dip 4 and dip 5 are selected with wavelength drift of $\Delta\lambda_{\mathrm{dip}\,A}$ and $\Delta\lambda_{\mathrm{dip}\,B}$, temperature sensitivity of K_{T_A} and K_{T_B}, and RI sensitivity of K_{n_A} and K_{n_B}, respectively. The amount of variation of n and T in the environment is Δn and ΔT. By bringing in the matrix

$$\begin{pmatrix} \Delta\lambda_{\mathrm{dip}\,A} \\ \Delta\lambda_{\mathrm{dip}\,B} \end{pmatrix} = \begin{pmatrix} K_{n_A} & K_{T_A} \\ K_{n_B} & K_{T_B} \end{pmatrix} \begin{pmatrix} \Delta n \\ \Delta T \end{pmatrix}. \tag{6}$$

The equation for the change in RI after temperature compensation is obtained as

$$\begin{pmatrix} \Delta n \\ \Delta T \end{pmatrix} = \begin{pmatrix} K_{n_A} & K_{T_A} \\ K_{n_B} & K_{T_B} \end{pmatrix}^{-1} \begin{pmatrix} \Delta\lambda_{\mathrm{dip}\,A} \\ \Delta\lambda_{\mathrm{dip}\,B} \end{pmatrix}. \tag{7}$$

Dip 4 and dip 5 were selected to demodulate the parameters. The minimum resolution of the spectrometer is 0.02 nm, which is substituted into (7) to obtain the resolution of the sensor. Within the range of 1.3333–1.4021 RIU

$$\begin{pmatrix} \Delta n \\ \Delta T \end{pmatrix} = \begin{pmatrix} -294.2 & 0.0526 \\ -263.9 & 0.0923 \end{pmatrix}^{-1} \begin{pmatrix} \Delta\lambda_{\mathrm{dip}\,A} \\ \Delta\lambda_{\mathrm{dip}\,B} \end{pmatrix}. \tag{8}$$

The maximum resolution of RI and temperature is 6×10^{-5} RIU and 0.046 °C, respectively, by solving the matrix equation. Meanwhile, within the range of 1.4021–1.4383 RIU

$$\begin{pmatrix} \Delta n \\ \Delta T \end{pmatrix} = \begin{pmatrix} -1230 & 0.0526 \\ -675.5 & 0.0923 \end{pmatrix}^{-1} \begin{pmatrix} \Delta\lambda_{\mathrm{dip}\,A} \\ \Delta\lambda_{\mathrm{dip}\,B} \end{pmatrix}. \tag{9}$$

At this time, the environmental RI and temperature resolution are 1×10^{-5} RIU and 0.14 °C, respectively. Hence, simultaneous measurement of RI and temperature with high sensitivity is realized.

Table III shows a comparison of the sensing performances between the PEM-ULPFG and the fiber sensors for dual-parameter sensing. The highest RI sensitivities of conventional MZI, LPFG, and ULPFG are usually lower than 1000 nm/RIU. The measurement range of these sensors is also limited. The maximum RI sensitivity of the proposed PEM-ULPFG is higher than the other sensors. In addition, the period number and the total length of the PEM-ULPFG are also shorter than the others.

V. CONCLUSION

In summary, we designed and fabricated an ULPFG based on periodically embedding MMF into SMF for high-sensitivity measurement of RI and temperature. The PEM-ULPFG shows five resonant dips in the wavelength range of 1000–1700 nm. The RI sensitivity is greatly enhanced by using the core diameter mismatch. Numerical simulation based on BPM is carried out to design, optimize, and verify the parameters and mode fields of the sensor. Experimental results show that the sensitivities of the different resonant dips vary from each other due to the different orders of the diffraction mode and cladding modes, the highest sensitivity of −294.2 nm/RIU (1.3333–1.4021 RIU) and −1230 nm/RIU (1.4021–1.4383 RIU) is achieved by tracing dip 4. The temperature response of dip 4 is also characterized to be 52.6 pm/°C. Dip 5 is used for measuring temperature with the temperature sensitivity of 92.3 pm/°C, which is about twice as much as that of dip 4. The different responses to the external changes of the dips obtained by the PEM-ULPFG make the proposed sensor competitive in the field of high sensitivity and dual-parameter sensing.

REFERENCES

[1] Q. Zhao, X. Liu, L. Ma, W. Zhao, and H. Wang, "Optical fiber pressure sensor based on F-P cavity in the oil and gas well," *IOP Conf. Earth Environ. Sci.*, vol. 64, no. 1, 2017, Art. no. 012007.
[2] S. Zhang et al., "Optimization and experiment of a miniature multimode fiber induced-LPG refractometer," *OSA Continuum*, vol. 2, no. 7, p. 2190, 2019.
[3] Y.-F. Hou et al., "Simultaneous measurement of pressure and temperature in seawater with PDMS sealed microfiber Mach–Zehnder interferometer," *J. Lightw. Technol.*, vol. 38, no. 22, pp. 6412–6421, Nov. 15, 2020.

[4] Y. Zhao et al., "Torsion, refractive index, and temperature sensors based on an improved helical long period fiber grating," *J. Lightw. Technol.*, vol. 38, no. 8, pp. 2504–2510, Apr. 15, 2020.
[5] L. Li et al., "Sagnac ring humidity sensor with a melting cone based on graphene properties," *IEEE Sensors J.*, vol. 21, no. 14, pp. 16061–16065, Jul. 2021.
[6] C. Jiang, Y. Liu, and C. Mou, "Polarization-maintaining fiber long-period grating based vector curvature sensor," *IEEE Photon. Technol. Lett.*, vol. 33, no. 7, pp. 358–361, Apr. 1, 2021.
[7] Z. Zhou, Z. Gong, B. Dong, S. Ruan, and C. C. Chan, "Enhanced sensitivity refractometer based on spherical Mach–Zehnder interferometer with side-polished structure," *IEEE Sensors J.*, vol. 21, no. 2, pp. 1548–1553, Jan. 2021.
[8] J. Barnes, S. Li, A. Goyal, P. Abolmaesumi, P. Mousavi, and H.-P. Loock, "Broadband vibration detection in tissue phantoms using a fiber Fabry–Pérot cavity," *IEEE Trans. Biomed. Eng.*, vol. 65, no. 4, pp. 921–927, Apr. 2018.
[9] S. Zhang, J. He, Q. Yu, and X. Wu, "Multi-scale load identification system based on distributed optical fiber and local FBG-based vibration sensors," *Optik*, vol. 219, Oct. 2020, Art. no. 165159.
[10] W. Ni et al., "Highly sensitive optical fiber curvature and acoustic sensor based on thin core ultralong period fiber grating," *IEEE Photon. J.*, vol. 9, no. 2, pp. 1–9, Apr. 2017.
[11] J. Zhang, S. Pu, J. Rao, and T. Yao, "Refractive index and temperature sensors based on no-core fiber cascaded with long period fiber grating," *J. Modern Opt.*, vol. 65, no. 9, pp. 1098–1103, May 2018.
[12] M. Shao, X. G. Qiao, X. L. Ren, and D. X. Yang, "Hybrid long-period fiber grating with multimode fiber core for refractive index measurement," *Chin. Phys. Lett.*, vol. 34, no. 11, 2017, Art. no. 114205.
[13] T. Zhu, Y. Song, Y. Rao, and Y. Zhu, "Highly sensitive optical refractometer based on edge-written ultra-long-period fiber grating formed by periodic grooves," *IEEE Sensors J.*, vol. 9, no. 6, pp. 678–681, Jun. 2009.
[14] S. Zhang et al., "A miniature ultra long period fiber grating for simultaneous measurement of axial strain and temperature," *Opt. Laser Technol.*, vol. 126, Jun. 2020, Art. no. 106121.
[15] X. W. Shu, L. Zhang, and I. Bennion, "Fabrication and characterisation of ultra-long-period fibre gratings," *Opt. Commun.*, vol. 203, nos. 3–6, pp. 277–281, 2002.
[16] Y. J. Rao, T. Zhu, and Q. J. Mo, "Highly sensitive fiber-optic torsion sensor based on an ultra-long-period fiber grating," *Opt. Commun.*, vol. 266, no. 1, pp. 187–190, 2006.
[17] Y. Liu and S. Qu, "Femtosecond laser pulses induced ultra-long-period fiber gratings for simultaneous measurement of high temperature and refractive index," *Optik*, vol. 124, no. 12, pp. 1303–1306, Jun. 2013.
[18] S. Zhang et al., "A compact ultra-long period fiber grating based on cascading up-tapers," *IEEE Sensors J.*, vol. 20, no. 15, pp. 8552–8558, Aug. 2020.
[19] W. Liu et al., "A new ultra long-period fiber grating for measuring torsional characteristics," *J. Modern Opt.*, vol. 66, no. 11, pp. 1215–1218, Jun. 2019.
[20] R. Chitaree and W. Talataisong, "The period sensitivity and modal sensitivity of optical fiber force sensor based on mechanical induced ultra-long period fiber grating," in *Proc. 15th Int. Conf. Opt. Commun. Netw. (ICOCN)*, Sep. 2016, pp. 1–3.
[21] S. Zhang, J. Yin, C. Zhang, J. Wu, and C. Miao, "Bending vector sensing based on periodic core-offset ultra-long period fiber grating," in *Proc. SPIE*, vol. 12057, 2021, pp. 614–621.
[22] B. Song et al., "Hydrophobin hgfi assisted immunobiologic sensor based on a cascaded taper integrated ultra-long-period fiber grating," *Biomedical Optics Exp.*, vol. 12, no. 5, pp. 2790–2799, 2021. [Online]. Available: https://www.ncbi.nlm.nih.gov/pubmed/34123504
[23] T. Zhu, Y. J. Rao, and J. L. Wang, "Characteristics of novel ultra-long-period fiber gratings fabricated by high-frequency CO_2 laser pulses," *Opt. Commun.*, vol. 277, no. 1, pp. 84–88, Sep. 2007.
[24] J. Li et al., "Long-period fiber grating cascaded to an S fiber taper for simultaneous measurement of temperature and refractive index," *IEEE Photon. Technol. Lett.*, vol. 25, no. 9, pp. 888–891, May 1, 2013.

Jiabin Wang was born in Jilin City, Jilin, China, in 1997. He received the B.S. degree in photoelectric information science and technology from Harbin Engineering University, Harbin, China, in 2019, where he is currently pursuing the Ph.D. degree with the College of Physics and Optoelectronic Engineering.

His research interests include optical sensing and sensors, fiber-optic miniaturized spectrometer, and astronomical photonics.

Jian Zhou was born in Chongqing, China, in 1998. He received the B.S. degree in physics from Chongqing Three Gorges University, Chongqing, in 2021. He is currently pursuing the M.S. degree with the College of Physics and Optoelectronic Engineering, Harbin Engineering University, Harbin, China.

His research interests include optical sensing and sensors.

Jiayu Hao was born in Harbin, Heilongjiang, China, in 1999. She received the B.S. degree in photoelectric information science and technology from the Harbin University of Science and Technology, Harbin, in 2021. She is currently pursuing the M.S. degree with the College of Physics and Optoelectronic Engineering, Harbin Engineering University, Harbin.

Her research interests include optical sensing and sensors.

Xinzhe Zeng, photograph and biography not available at the time of publication.

Wenhuan Chen, photograph and biography not available at the time of publication.

Yue Liu, photograph and biography not available at the time of publication.

Haoran Meng, photograph and biography not available at the time of publication.

Jinghua Sun, photograph and biography not available at the time of publication.

Tao Geng, photograph and biography not available at the time of publication.

Weimin Sun, photograph and biography not available at the time of publication.